Citation (APA)
D'Angelo, C. D., Buszek, M. J., Terra, W., & Sciacchitano, A. (2026). On-site investigation of running aerodynamics. *Experiments in Fluids: experimental methods and their applications to fluid flow*, *67*. https://doi.org/10.1007/s00348-026-04204-3

Experiments in Fluids (2026) 67:76
https://doi.org/10.1007/s00348-026-04204-3

RESEARCH ARTICLE

On-site investigation of running aerodynamics

C. D'Angelo[1] · **M. Buszek**[2] · **W. Terra**[2] · **A. Sciacchitano**[2]

Received: 16 December 2025 / Revised: 16 February 2026 / Accepted: 27 February 2026

Abstract

We present an on-site aerodynamic investigation of runners through the Ring of Fire (RoF) methodology. The Lagrangian Particle Tracking (LPT) technique is used with helium filled soap bubbles as tracer particles and LED illumination; the acquired time-resolved data are processed through the Shake-the-Box (STB) algorithm. The RoF measurements are performed with six athletes running at an average speed of 8 m/s, resulting in a Reynolds number of 2×10^5, based on the shoulder width. While existing studies largely focus on numerical simulations and experimental measurements performed on static human models, the present analysis investigates the wake flow topology of moving runners, thus addressing a significant gap in the literature. Specifically, the ensemble-averaged streamwise velocity and vorticity fields, along with the pressure coefficient distribution in the wake, are investigated. The results reveal that, close to the athlete, the wake shape closely resembles the runner's body outline, with the torso area exerting the greatest influence. Moreover, in the near wake, a downwash effect from the head and an upwash effect from the hips are identified. This flow behaviour is further supported by the streamwise vorticity distribution analysis, which confirms the consistent formation of vortical structures across different athlete passages. Additionally, the aerodynamic drag is evaluated by applying the momentum conservation within a control volume containing the athlete. The results, presented in terms of the drag area, reveal that the overall drag area is largely independent of the control volume length, while the individual drag area contributions vary along the wake, with the greatest variations detected close to the athlete. The computed drag areas are 30–40% lower than most of the values reported in previous experimental and numerical studies, a difference attributed to the higher realism of the experimental measurements performed in this study, which capture the fully unsteady nature of the running motion. Moreover, a linear increase in the drag area with the athlete's height squared is found.

1 Introduction

The role of aerodynamics is significant in many speed sports, in which fractions of a second can make the difference between losing and winning a competition. In high-speed sports, the aerodynamic drag is usually the greatest resistive force, accounting for up to 80% of the total drag in speed skating (Sætran and Oggiano 2008) and 90% in road cycling (Gibertini and Donato 2008). The importance of estimating the aerodynamic drag and understanding the flow field around athletes in elite speed sports is therefore evident. This applies also to sprinting, where the aerodynamic drag influences the acceleration and top speed of the athletes, thus affecting their overall race time.

According to Hill (1928), the aerodynamic drag accounts for at most 5% of the total drag of a runner, while Schickhofer and Hanson (2021) proved that the aerodynamic drag consumes approximately 7–9% of a sprinter's total mechanical power in the velocity range of 30 to 36 km/h; such percentage increases with increasing athlete velocity. Despite the relatively small contribution of the air resistance to the overall resistive force, its reduction can lead to improved performance (Chowdhury et al. 2010; Brownlie et al. 2016).

Some numerical and experimental analyses have explored running aerodynamics. Zhang et al. (2023) performed both wind tunnel tests and numerical simulations to investigate the aerodynamic drag reduction in race walking formations, using static models; their findings highlight the presence of a recirculation region behind the athlete, with the flow separating at the head and generating a downwash along the back. Furthermore, the wake is primarily influenced by

---

✉ C. D'Angelo
cri.dan99@gmail.com

[1] Department of Industrial Engineering, University of Naples "Federico II", Naples, Italy

[2] Aerospace Engineering Department, Delft University of Technology, Delft, The Netherlands

the torso, shoulders and hips, while the head and the legs exert minimal effect owing to their narrower cross-section. On the other hand, Schickhofer and Hanson (2021) performed numerical simulations of stationary human models to investigate the aerodynamic features of running formations; their results show an asymmetric velocity distribution in the wake, due to differing arm positions between the right and left side; the same consideration can be drawn from the results of Zhang et al. (2023). Also Beaumont et al. (2021) numerically investigated the flow field of drafting formations in running, using static models; their findings show that the low pressure region behind an individual runner extends up to approximately 1 m, consistent with the results of Schickhofer and Hanson (2021). Similarly, Forte et al. (2022) employed CFD analyses to estimate the aerodynamic drag in walking, running and sprinting, for velocity values ranging between 0.28 and 11.11 m/s, concluding that the pressure drag dominates the total air resistance.

Nevertheless, as also highlighted in the numerical study of Hu et al. (2026), existing numerical analyses of running aerodynamics are typically limited to fixed athletes' postures and do not account for the unsteady effects introduced by the actual running motion. Therefore, such quasi-steady analyses only explain running aerodynamics to some extent. Kim et al. (2023) sought to overcome the limits of analysing a static model by simulating the static runner in two distinct phases, the take-off phase (back foot leaving the ground) and the touchdown phase (front foot landing on the ground). Their analysis reveals that, although in both phases flow separation occurs behind the athlete, different flow structures are generated in the runners' wake, therefore resulting in varying drag forces between the take-off and touchdown phases. On the other hand, Pecchiari et al. (2023) experimentally determined the aerodynamic drag of a runner moving on an instrumented treadmill mounted in a wind tunnel. They found that the aerodynamic drag of runners linearly increases with the square of the runners' height. However, no analysis of the flow field around the moving runners was performed in order to understand if other factors, apart from the athlete height, may affect the runner's aerodynamic drag.

To the best knowledge of the authors, none of the experimental and numerical studies on running aerodynamics measured the flow field around a moving athlete, due to the difficulties encountered for such analyses. Nonetheless, running is a dynamic sport in which the posture of the athlete changes continuously. Therefore, the aim of the current work is to measure and analyse the flow field around a sprinter and to assess the aerodynamic drag acting on the athlete. For this purpose, the Ring of Fire (RoF) approach is used. Such technique has already been employed for cycling (Spoelstra et al. 2019), speed skating (Spoelstra et al. 2023) and in the automotive industry (Huttig et al. 2023). It employs large-scale Lagrangian Particle Tracking (LPT) to measure the flow field prior and after the passage of an athlete or object. This work provides the first comprehensive visualization of the wake generated by a moving sprinter and a detailed assessment of the corresponding aerodynamic drag, expressed in terms of the drag area. Additionally, the wake information is used to discuss the potential drag reduction of drafting formations and to analyse the effects of the athletes' height on the drag area.

2 Experimental setup and procedure

The experiments were conducted in an indoor sprint hall at the Omnisport sport facility, located in Apeldoorn, the Netherlands. The hall features six lanes, each measuring 1.2 m in width and 80 m in length. Six junior athletes, acting on the Dutch sub-elite level, participated in the experimental campaign, comprising four males (height ranging from 1.80 to 1.85 m) and two females (height range of 1.65–1.70 m). Each participant signed an informed consent form prior to the experiments and performed five tests while wearing low-drag tight-fitting sprint suit. The velocity of the athletes U_A was measured using a laser Doppler device (LAVEG LDM 300C by Jenoptik) (Ashton and Jones 2019); the average running speed was approximately 8 m/s, with a standard deviation of 0.27 m/s, corresponding to a Reynolds number of 2×10^5, based on the shoulder width ($D \approx 0.4m$).

2.1 Experimental apparatus and data reduction

A schematic of the experimental apparatus employed is depicted in Fig. 1, while an actual photograph of the setup is shown in Fig. 2.

In order to measure and analyse the flow field prior and after the passage of the sprinters, large-scale Lagrangian Particle Tracking is employed according to the Ring-of-Fire concept; sub-millimetre Helium-filled soap bubbles (HFSB) are used as flow tracers (Scarano et al. 2015), injected through a multi nozzle seeding rake, also employed by Spoelstra et al. (2019); as shown in Fig. 1 and Fig. 2, the seeding rake is located approximately at the entrance of the tunnel. For the performed experiments, 100 nozzles out of 200 have been used. The flow rates of helium, air and bubble fluid solution are regulated via a custom-made Fluid Supply Unit.

The flow tracers are generated and confined within a tunnel of $5 \times 4 \times 2.5$ m^3 (see Fig. 1 and Fig. 2). The blockage ratio, defined as the ratio between the frontal area of the athlete and the cross-sectional area of the tunnel, is estimated to be approximately 4%, with slight variations among athletes and throughout the running motion. The measurement region is placed at approximately half of the duct; the origin of the reference system (X, Y, Z) employed in the current

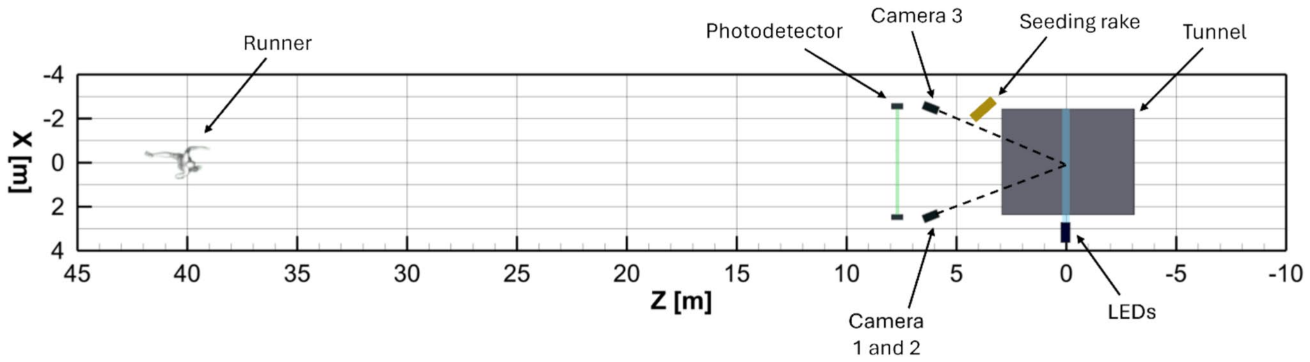

Fig. 1 Schematic of the experimental apparatus

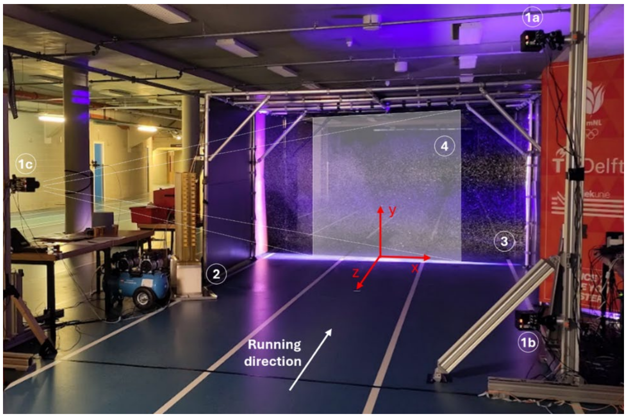

Fig. 2 Photograph of the experimental apparatus; CMOS cameras (1a, 1b, 1c, respectively camera 1, 2 and 3), seeding rake (2), HFSB (3), measurement region (4). The LEDs are not visible in the picture because they are covered by the banner on the right

study is located on the ground, in correspondence of the centre of the middle lane, as illustrated in Fig. 2. The XY plane of such reference system is positioned on the mid-plane of the measurement region, while the Z direction is aligned with the direction of the athlete's motion but is oriented opposite to the running direction (see Fig. 2). The notation adopted for the velocity components is defined according to the reference system employed. The distance between the starting position of the athletes and the mid-plane of the measurement region is equal to 40 m (see Fig. 1). Therefore, considering the mathematical-physical model of the 100 m dash proposed by Mureika (2001), the maintenance phase of the sprint race is analysed in the current work.

The HFSB are illuminated by four pulsed LEDs (LaVision Flashlight 300), which are installed on top of each other just outside of the duct (see Fig. 1). A rectangular slid (20 cm × 200 cm) in the wall of the duct allows to produce a light beam approximately 30 cm thick. The field of view of $2.7 \times 2.7 \times 0.3$ m^3 is imaged by three Photron MINI AX 100 cameras (CMOS, 1024×1024 pixels, pixel pitch of 20 µm, 12 bits) equipped with Nikon 50 mm objectives at f/5.6. The cameras were geometrically calibrated using the pinhole camera model and a custom 3D calibration plate; afterwards, a volume self-calibration has been performed (Wieneke 2008). The optical magnification is approximately 0.008, resulting in a digital image resolution of 2.51 mm/pixel. The number of particles per pixel (ppp) ranges between 0.02 and 0.035, corresponding to a particle concentration of 0.01–0.02 particles/cm^3. The highest density is observed before the athletes' passage, where the seeded streamtube remains unaffected by the wake of the athletes, whereas the lowest ppp appears in the runners' wake. The average particle image peak intensity is approximately equal to 200 counts over a background intensity of about 10 counts, resulting in an image signal-to-noise ratio of 20.

Before the passage of the athlete, the HFSB accumulate for approximately 15 s. The tracer production is paused prior to the passage of the runner, in order to allow the HFSB to settle. Figure 3 (left) depicts a sample of the resulting, rather uniform seeding distribution. The image acquisition is triggered by a photoelectric sensor, which is positioned at a distance of 7 m from the measurement volume (see Fig. 1). A total of 1000 images is acquired at a frequency of 400 Hz, with an LED pulse duration of 250 µs. Therefore, the total distance travelled by a runner during an image acquisition is of approximately 20 m, allowing flow measurements up to 7 m in front and 13 m in the back of the runner. The LaVision DaVis 10 software is used for image acquisition and processing.

The equipment employed and the experimental parameters are summarized in Table 1 and Table 2, respectively.

2.2 Data processing and uncertainty analysis

The acquired data has been processed with the software DaVis 10 from LaVision GmbH. First, image

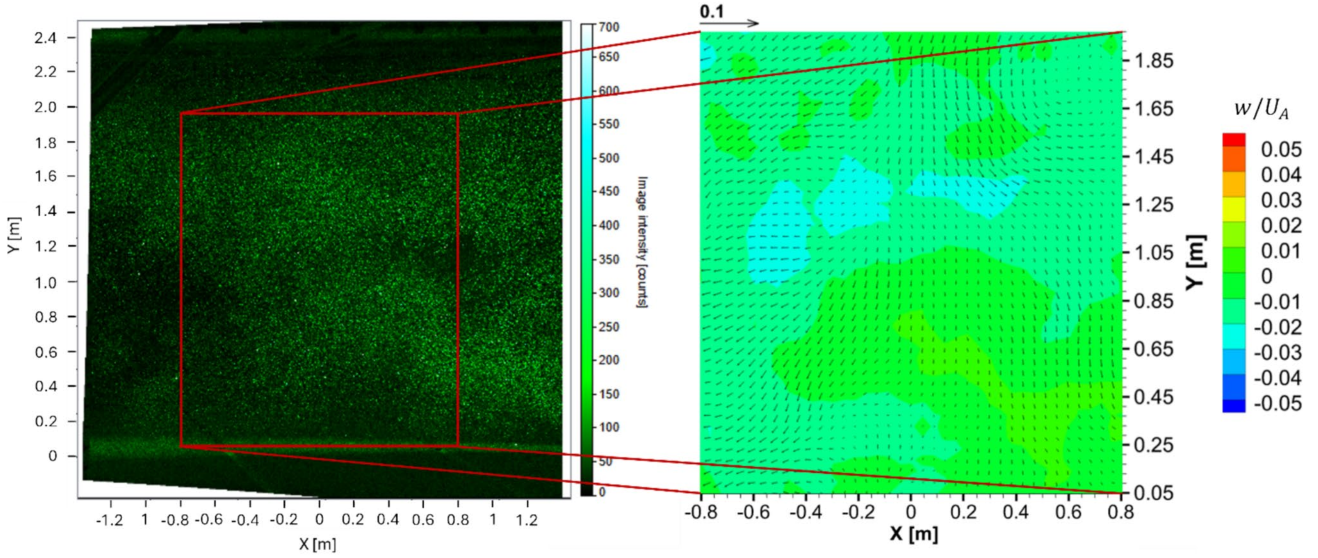

Fig. 3 Seeding distribution prior to the athlete's passage (left) and in-plane streamwise velocity vector field from an instantaneous run (right)

Table 1 Equipment

Purpose	Instrument	
Imaging	Cameras	3 × Photron MINI AX 100 (CMOS, 1024 × 1024 pixels, pixel pitch of 20 µm, 12 bits)
	Objectives	3 × Nikon $f = 50$ mm, $f\# = 5.6$
Illumination	LEDs	4 × LaVision FlashLight 300
Seeding	Tracer particles	Helium filled soap bubbles, median diameter of 0.4 mm
	Seeding system	100 generators

Table 2 Imaging and acquisition parameters

Purpose	Parameter	Value
Field of view	X (width)	2.7 m
	Y (height)	2.7 m
	Z (thickness)	0.3 m
Imaging	focal length	50 mm
	$f_{\#}$	5.6
	Magnification factor	0.008
	Digital image resolution	2.51 mm/px
	Acquisition frequency	400 Hz
Illumination	Pulse duration	250 µs
Seeding concentration	Particles per pixel (ppp)	0.02–0.035
	Particle concentration	0.01–0.02 particles/cm^3

preprocessing is performed by subtracting the time-minimum intensity over a kernel of 31 consecutive images in order to reduce the camera background noise. Afterwards, the flow velocity is obtained through Lagrangian Particle Tracking, using the Shake-the-Box algorithm (Schanz et al. 2016). Through a binning procedure (Agüera et al. 2016), the Lagrangian flow information is converted into a Cartesian grid having a sub-volume size of 170 mm with 75% overlap. The resulting vector spacing is 42.5 mm. To avoid outliers on the boundaries of the domain, binning was applied within a region of 1.6 × 1.8 m^2 in the XY plane.

A snapshot of the streamwise velocity distribution prior to the passage of the athlete is depicted in Fig. 3 (right). The average speed of the flow is about 0.3% of the athletes' average speed. Due to the external conditions and the seeding injection, the flow before the passage of the athlete is characterized by a velocity w_u which, in general, is non-zero, non-uniform and non-stationary. This factor contributes to the overall momentum budget (Terra et al. 2018), and is therefore taken into account for the computation of the aerodynamic drag, as discussed in Sect. 2.3.

In order to gain a statistically significant understanding of the flow field generated by a sprinter, before converting the Lagrangian data into a Cartesian grid, particle tracks from runs in which the athlete passed through the measurement domain in the same phase are averaged. The phase-averaging procedure is as follows: (1) for each run normalize the obtained velocity by the athlete's speed (accounting for variations in crossing speed); (2) convert time into the spatial Z-coordinate using the relation $Z = Z_0 + \left|U_A\right|t$, where Z_0 is selected so that $Z=0$ corresponds to the moment the athlete's left foot has just passed through the illuminated region (see Fig. 4, left); (3) align the wake information among the runs along the X-axis (lateral direction), according to the lateral position in which the athlete passes through the measurement domain; (4) convert the entire ensemble of Lagrangian data onto the Cartesian grid by means of a binning procedure, as explained in Agüera et al. (2016). It is worth noting that, although the averaging procedure was based on a limited number of repeated runs per athlete (five passages), the flow statistics obtained were consistent across all repetitions, supporting the robustness of the results.

A snapshot of the runner passing through the measurement domain seeded with HFSB and the result obtained through the application of the particle tracking algorithm are shown in Fig. 4 (left and right, respectively).

The uncertainty of the streamwise velocity component w has been computed as the standard deviation of such component divided by the number of particles tracks found within each bin and has been estimated to be 2.5% of the athletes' speed in the wake, while being approximately 0.1% of the athlete's speed in the freestream and at the domain boundaries in the wake.

2.3 Drag estimation

The drag force experienced by a body moving through a fluid is typically represented by Eq. 1:

$$D = \frac{1}{2}\rho {U_A}^2 C_D A \tag{1}$$

where D is the overall drag force, $\frac{1}{2}\rho {U_A}^2$ the free-stream dynamic pressure, C_D the drag coefficient and A a reference area which, in the current analysis, is considered to be the projected frontal area of the runners when they are passing through the illuminated region.

The RoF concept is applied for the determination of the aerodynamic drag (Spoelstra et al. 2019); more in detail, the aerodynamic drag of the runners is obtained from the large-scale LPT measurements invoking the conservation of momentum in a control volume surrounding the athlete and moving with him. To simplify the formulation of the problem, a Galilean transformation (Arnol'd 2013) is applied in order to represent velocity and momentum in the reference frame moving with the athlete (X',Y',Z'), whose speed is U_A, assumed to be constant in the laboratory reference frame. Since the air motion induced by external disturbances in the environment cannot be neglected (Terra et al. 2018), the chaotic velocity upstream of the passing athlete w_u must be taken into account in the momentum conservation. After the passage of the athlete, the flow velocity exhibits a distribution w_w, which evolves along the wake.

To compute the aerodynamic drag of the runners, the conservation of momentum is applied across two surfaces:

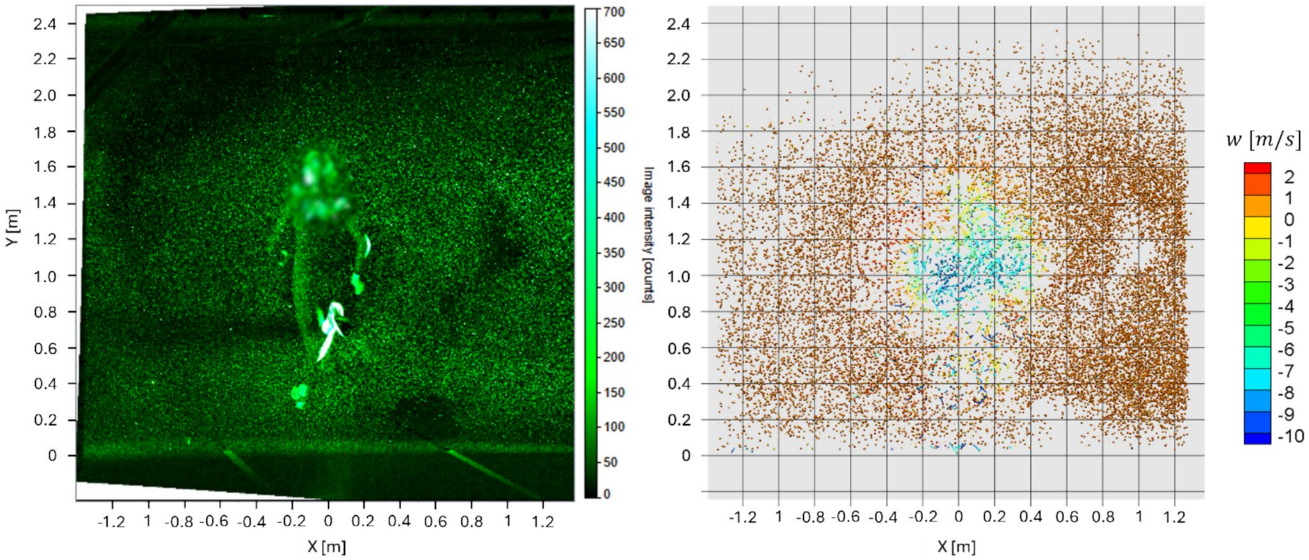

Fig. 4 Snapshot of the runner passing through the measurement domain seeded with HFSB (left) and particle tracks color-coded by streamwise velocity (right)

one upstream and one downstream of the athlete's passage, with respective areas A_u and A_w both perpendicular to the direction of the runner's motion. If the control surfaces A_u and A_w are far enough from the analysed body, due to the high Reynolds number of the problem, the viscous stress can be neglected in the drag evaluation (Kurtulus et al. 2007). Therefore, the phase-averaged drag $\overline{D}(z)$ is calculated as the sum of the momentum term, pressure term and Reynolds stress term, as written in Eq. 2.

$$\bar{D}(z) = \underbrace{\rho \iint_{A_u} \left(\overline{w_u} - U_A\right)^2 dA - \rho \iint_{A_w} \left(\overline{w_w} - U_A\right)^2 dA}_{Momentum\ term} + \underbrace{\iint_{A_u} \left(\overline{p_u} - p_\infty\right) dA - \iint_{A_w} \left(\overline{p_w} - p_\infty\right) dA}_{Pressure\ term} - \underbrace{\left(\iint_{A_w} \overline{w_w}^2 dA - \iint_{A_u} \overline{w_u}^2 dA \right)}_{Reynolds\ stress\ term} \qquad (2)$$

ρ is the air density, p_∞ is the freestream pressure, p_u and p_w are the pressure distributions upstream and downstream of the athlete, respectively, obtained from the velocity field by resolving the Poisson equation for pressure (Oudheusden 2013); Neumann boundary conditions are applied and the measured quiescent air pressure is used as a reference to scale the resulting pressure distributions. The Reynolds stress term is computed from the surface integrals of w'_w and w'_u which are, respectively, the streamwise velocity fluctuations in the wake and upstream of the athlete's passage. Moreover, since Eq. 2 can only be applied if the mass flow is conserved across the surfaces A_u and A_w, the inlet surface A_u is shrunk from the outer edges, starting from the size of the outlet surface A_w. More in detail, to identify the surface A_w, an enclosure of the wake structure and a subsequent contouring of the inlet plane have been applied, following the approach of Spoelstra et al. (2021).

For individual runs, the Reynolds stress term is not present, therefore the instantaneous drag is computed as the sum of the momentum term and the pressure term only, where the phase-averaged quantities in Eq. 2 are replaced with the corresponding instantaneous ones.

Following Crouch et al. (2014), in the current work the aerodynamic drag results are presented in terms of the drag area C_DA, defined as the product of the drag coefficient and the reference area (or ratio between drag force and dynamic pressure), expressed in square meters. This choice is motivated by the practical difficulty of accurately measuring the projected frontal area of the athletes, as their body position continuously changes throughout the motion. Moreover, this approach enables direct comparison with running drag results found in the literature, where projected frontal area data may not be available.

Furthermore, the uncertainty associated with the aerodynamic drag estimation obtained through the Ring of Fire methodology has been thoroughly assessed by Spoelstra et al. (2021), who reported an overall uncertainty within 5% of the measured drag area.

3 Results and discussion

In this section, an analysis of the flow field in the wake of a single athlete is presented, followed by an examination of the drag area evolution along the wake.

3.1 Quantitative visualization of the runner's wake

The flow topology in the wake of the runner is investigated through the analysis of streamwise velocity and vorticity distributions, along with the pressure coefficient distribution, in planes perpendicular to the runner's motion (i.e. XY planes). The results presented are obtained by averaging five runs of the same athlete.

3.1.1 Wake flow velocity

In Fig. 5, the ensemble-averaged 3D streamwise velocity field in the wake of the athlete is illustrated. The data shown is the normalized streamwise velocity component w/U_A, being U_A the speed of the athlete. Moreover, isosurfaces along the wake at 10% and at 50% of the normalized streamwise velocity are shown in orange and green, respectively.

The analysis of Fig. 5 reveals that, close to the athlete, the wake shape visibly resembles the runner's body, with the torso area causing the greatest velocity deficit. The right leg also affects the wake shape as it begins to move forward, while the left leg has a negligible effect. As the distance from the runner increases, the wake becomes shorter in height and broader in width. Eventually, the streamwise velocity deficit splits into two regions of peak velocity, with a noticeable decrease in the velocity values between these two peaks. This pattern emerges around the height of the arms and persists until the wake dissipates. One possible explanation for the wake splitting into two parts is the residual velocity of the legs and the arms, which move at a faster speed than the body. Therefore, compared to other areas, these regions with higher initial velocity may exert an influence that persists over a greater distance in the wake.

In Fig. 6, the side view (YZ plane at $X = 0$ m) and the top view (XZ plane at $Y = 0.8$ m) of the ensemble-averaged normalized streamwise velocity w/U_A in the wake of the athlete

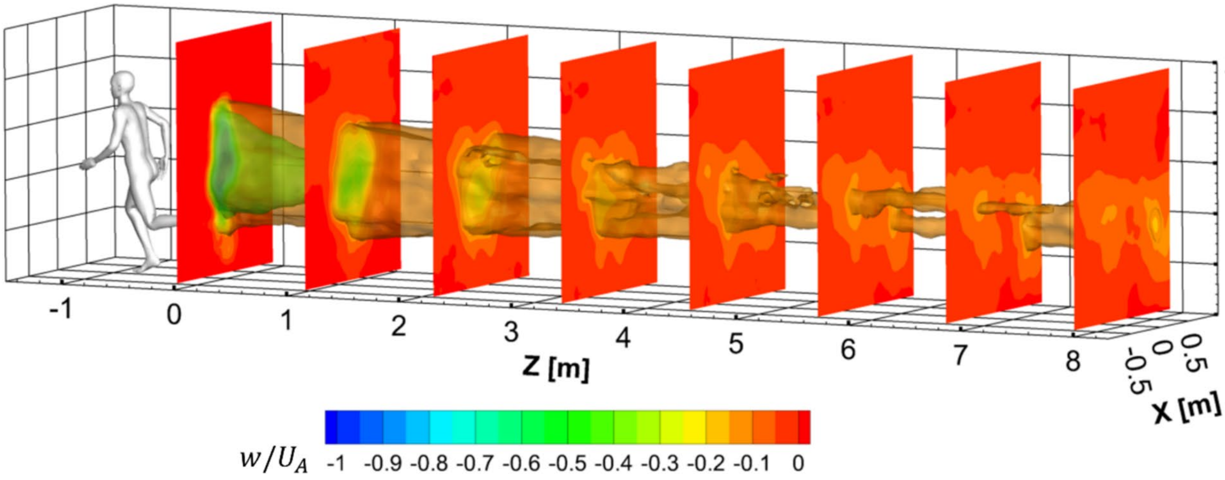

Fig. 5 Ensemble-averaged 3D streamwise velocity field in the wake of the athlete and isosurfaces along the wake at 10% and 50% of w/U_A

are depicted; in-plane velocity vectors are also shown, thus providing further insight into the wake flow characteristics. These vectors highlight the presence of upwash and downwash effects in proximity of the athlete (see Fig. 6, top), as well as lateral entrainment from the sides (see Fig. 6, bottom). Moreover, the absence of reverse flow (i.e. regions where the flow velocity exceeds the runner's speed) in the figure suggests that the recirculation region extends to less than 0.8 m behind the athlete.

As also found by Schickhofer and Hanson (2021), the runner's wake exhibits a relevant streamwise velocity deficit which, in the analysed case, extends up to a distance of approximately 8 m behind the athlete. In light of this observation, the distributions of the normalized streamwise velocity w/U_A, of the streamwise vorticity ω_z and of the pressure coefficient C_p are analysed up to a distance $Z=8$ m. Furthermore, the top view of the ensemble-averaged w/U_A (Fig. 6, bottom) reveals an asymmetry in the wake flow, attributed to differences in arm and leg positioning between the left and right sides. This asymmetry results in a slight deflection of the wake to the left (i.e. along the negative X direction), which emerges at downstream distances ranging

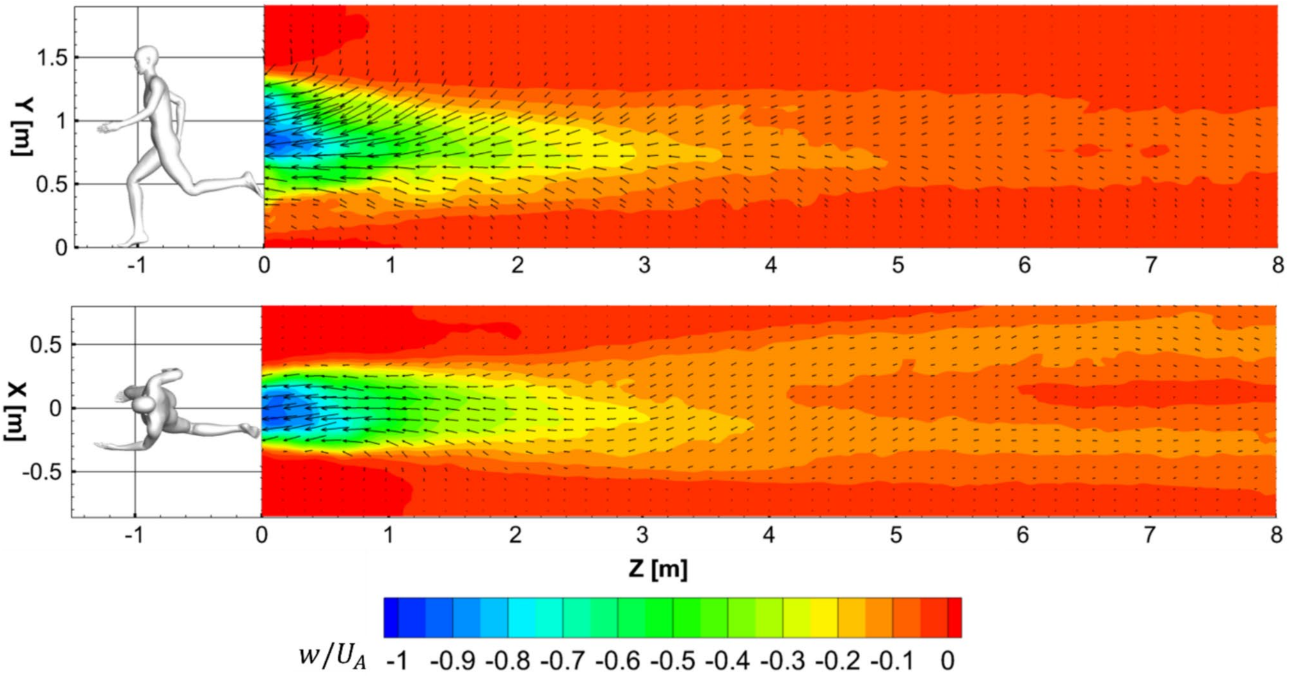

Fig. 6 Side view (YZ plane at $X=0$ m) and top view (XZ plane at $Y=0.8$ m) of the ensemble-averaged normalized streamwise velocity w/U_A past the athlete

between 2 and 4 m. Such phenomenon is attributed to the forward motion of the left arm, in agreement with the findings of Schickhofer and Hanson (2021) and those of Zhang et al. (2023).

In Fig. 7, the evolution of the ensemble-averaged w/U_A in the XY planes along the wake at $Z = 0$, 0.25, 0.5, 1, 1.5, 2, 4, 6 and 8 m is depicted. Furthermore, to uniquely identify the distinct characteristics of the wake flow, the athlete's outline is superimposed on the distribution of w/U_A at $Z = 0$ m. To enhance the clarity of the visualization, on the top-left of Fig. 7 the schematic of the runner and the examined XY planes in the wake within the YZ plane are illustrated; each plane considered along the Z direction is marked by a red line.

From the analysis of Fig. 7, a downwash from the head is identifiable in the near wake; such phenomenon has also been found in the literature (Zhang et al. 2023; Kim et al. 2023). Indeed, the results of Zhang et al. (2023) and of Kim et al. (2023) show that the runner's head exhibits a large region of attached flow after which separation occurs, therefore generating a downwash flow developing along the back of the athlete. This phenomenon is similar to that observed for a truncated cylinder: in the near-wake region of the latter, a downwash flow is generated in proximity of the free end, it persists in the streamwise direction and moves down towards the central region of the wake (Rostamy et al. 2012; Krajnović 2011). Furthermore, in the near wake, the flow is also influenced by the shoulders and hips. The shoulders generate a sidewash flow directed toward the central region of the athlete's back, thus contributing to the downwash originating from the head. Moreover, although less significant than the downwash, an upwash is also visible downstream of the upper legs, caused by the air passing in between the thighs.

In addition, Fig. 7 shows that in the near proximity of the runner, i.e. for Z ranging between 0 and 0.5 m, the streamwise velocity deficit exhibits the highest values downstream of the torso, with additional contributions from the arms and a minor contribution from the legs. These findings align with those reported in the literature (Zhang et al. 2023). However, differently from the findings of previous numerical studies (Schickhofer and Hanson 2021; Zhang et al. 2023; Beaumont et al. 2021), the velocity deficit downstream of the standing leg is small, in particular behind the calf region. In the present phase of the stride ($Z = 0$), the right foot of the runner is standing on the floor and is therefore stationary relative to the air. The velocity of the right leg linearly increases at increasing distance from the floor until, at the thighs, it is the same as that of the torso (~ 8 m/s). The relative low velocity of a large part of the standing leg explains the low velocity deficit downstream of it. Conversely, at $Z = 0$, the left leg is moving at a speed that exceeds that of the torso. Hence, its wake is clearly visible immediately at $Z = 0$ m. Because this leg is retracted while moving forward, the wake region influenced by the left leg is relatively small. Therefore, the analysis of Fig. 7 reveals that the legs are clearly responsible for significant asymmetries in the general wake flow topology. Further downstream, for distances ranging between $Z = 1$ m and $Z = 2$ m, the wake contracts vertically while expanding horizontally, with its development preferentially oriented along the diagonal direction at 45°. Afterwards, for $Z > 4$ m, the wake structure splits into two separate regions, one located on the left side (negative X direction) and the other on the right side (positive X direction). These regions, attributed to the motions of the arms, exhibit higher streamwise velocity values, while in the area between them w/U_A recovers to freestream levels. Furthermore, Fig. 7 shows that the streamwise velocity deficit reduces as the distance behind the athlete increases.

Overall, these results highlight that, in the near wake, the flow topology is strongly influenced by the instantaneous body posture, with marked asymmetries directly associated with the motion of individual limbs. Further downstream, as the wake develops and turbulent mixing increases, the flow progressively loses sensitivity to the exact limb configuration and approaches a statistically averaged wake.

To further analyse the wake flow characteristics and their aerodynamic implications, the velocity deficit in the runner's wake is examined. Specifically, the latter can be quantified by analysing the evolution of the streamwise velocity value along the Z direction. Figure 8 (right) illustrates the evolution of the minimum value of w/U_A along the wake and of the average value of w/U_A computed across a rectangular area centred around the athlete's torso (see Fig. 8, left). The figure shows that, in proximity to the athlete, the minimum value of w/U_A is slightly lower than the runner's speed, while $(w/U_A)_{mean}$ is approximately 80% of the athlete's average speed. Both these values increase up to $Z \cong 5$ m, beyond which $(w/U_A)_{\mathrm{min}}$ and $(w/U_A)_{\mathrm{mean}}$ reach a plateau at around 10% and 5% of the athlete's speed, respectively. This analysis is particularly relevant for determining the optimal positioning of a drafting runner relative to the front runner to gain aerodynamic advantages, an aspect that will be further analysed later in the discussion.

3.1.2 Vorticity fields

Beyond the streamwise velocity distribution and the velocity deficit in the runners' wake, an analysis of the vortical structures generated along the wake is essential for gaining a deeper understanding of the wake flow topology. Since the primary vortical structures mainly develop along the Z direction, the evolution of the streamwise vorticity component ω_z is analysed.

Figure 9 illustrates the evolution of the ensemble-averaged ω_z in the XY-planes at $Z = 0$, 0.25, 0.5, 1, 1.5, 2, 4, 6

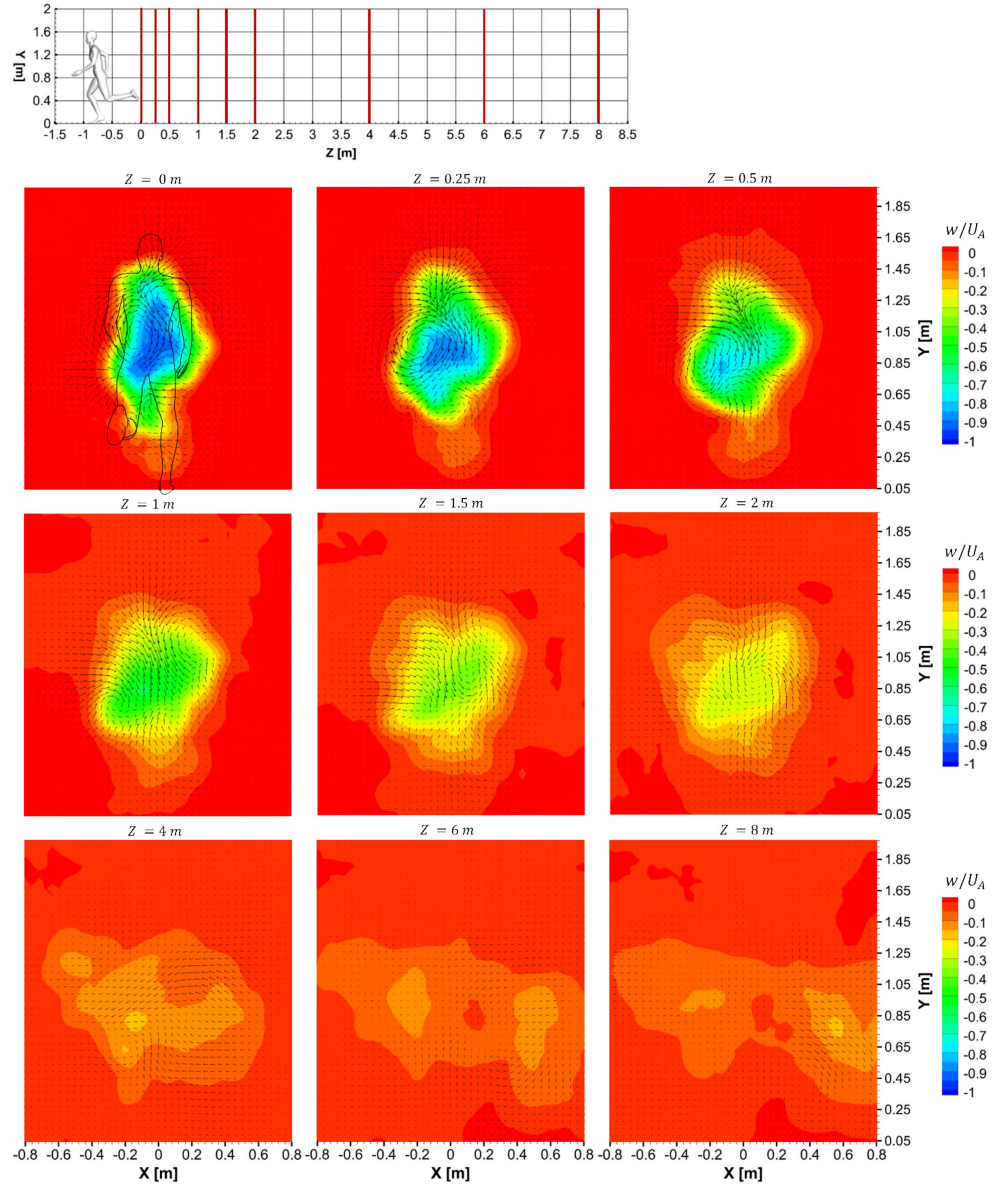

Fig. 7 Evolution of the ensemble-averaged non-dimensional streamwise velocity component w/U_A in the XY-plane along the wake, at $Z=0$, 0.25, 0.5, 1, 1.5, 2, 4, 6 and 8 m

and 8 m, along with in-plane vectors of the velocity field. The vorticity ω_z has been non-dimensionalized with respect to the athlete's speed U_A and the shoulder width D. Furthermore, since the vorticity dissipates with increasing the distance behind the runner, the range of ω_z in the colorbars has been varied with the increase of Z. It is also noteworthy that the described vorticity structures are consistently observed across the various athlete passages and can be directly attributed to the corresponding body parts responsible for their generation. Indeed, vorticity structures are observed in the near wake of the athlete, and their positional evolution and variation are examined in relation to the athlete's body parts. To enhance the clarity of the discussion, the vortical structures described in the text have been highlighted in Fig. 9 by circling and labelling them.

At $Z=0$ m, a significant rotational region forms in correspondence of the left side of the torso (LS). This vortical structure is likely driven by the interaction between the forward motion of the left arm and the athlete's back. Similarly, the motion of the right arm generates a vortex between the right side of the torso and the right arm itself (RS). The LS vortex gradually decreases in intensity from $Z=0$ m to $Z=0.5$ m, eventually splitting into two distinct vortices, LS1 and LS2, at $Z=1$ m. By $Z=1.5$ m, LS1 further divides into LS1a and LS1b. These newly formed vortices, along with LS2, dissipate beyond $Z=2$ m, due to the turbulence in the athlete's wake.

Furthermore, at $Z=0$, two counter-rotating vortices are observed in the upper part of the athlete's back (RU) and on the left side of the neck (LU). The RU vortex exhibits greater intensity compared to the LU vortex. Moreover, the LU vortex begins to dissipate at $Z=0.25$ m, while the RU vortex persists further downstream, until it merges with the RS vortex, thus generating the RSU vortical structure at $Z=0.5$ m. The latter persists in the wake up to $Z=1$ m until, at $Z=1.5$ m, it splits into two distinct vortices, labelled as RSU1 and RSU2. It is moreover remarked that the intensity of the vortical structures LS, RU and RS exhibits a significant decrease for $Z>1$ m. The analysis of Fig. 9 also reveals that these three vortical structures contribute to the generation of a downwash along the athlete's back, which does not follow a linear trajectory but instead curves initially to the left, then to the right, and ultimately develops along the left side at an approximate 45° angle.

Additional vortical structures can be identified from the analysis of the streamwise vorticity distribution in the runner's wake. Nevertheless, the vortical structures described below exhibit lower intensity compared to those previously discussed and therefore appear to exert a lesser influence on the wake flow.

Indeed, at $Z=0$ m, two additional pairs of counter-rotating vortices are formed in proximity of the right hip (RH and RHC). Specifically, the RH vortex contributes to the downwash along the athlete's back, while RHC contributes to the upwash effect generated by the motion of the legs. Moreover, in the near wake, the circulation regions generated by the motion of the left and right leg (LL and RL, respectively) are observed. Both this vortical structures contribute to the aforementioned upwash effect. Differently from LS, RU and RS, the vortical structures RH, RHC, LL and RL dissipate at shorter distances from the athlete while interacting with each other. Consequently, due to the uncertainty in the

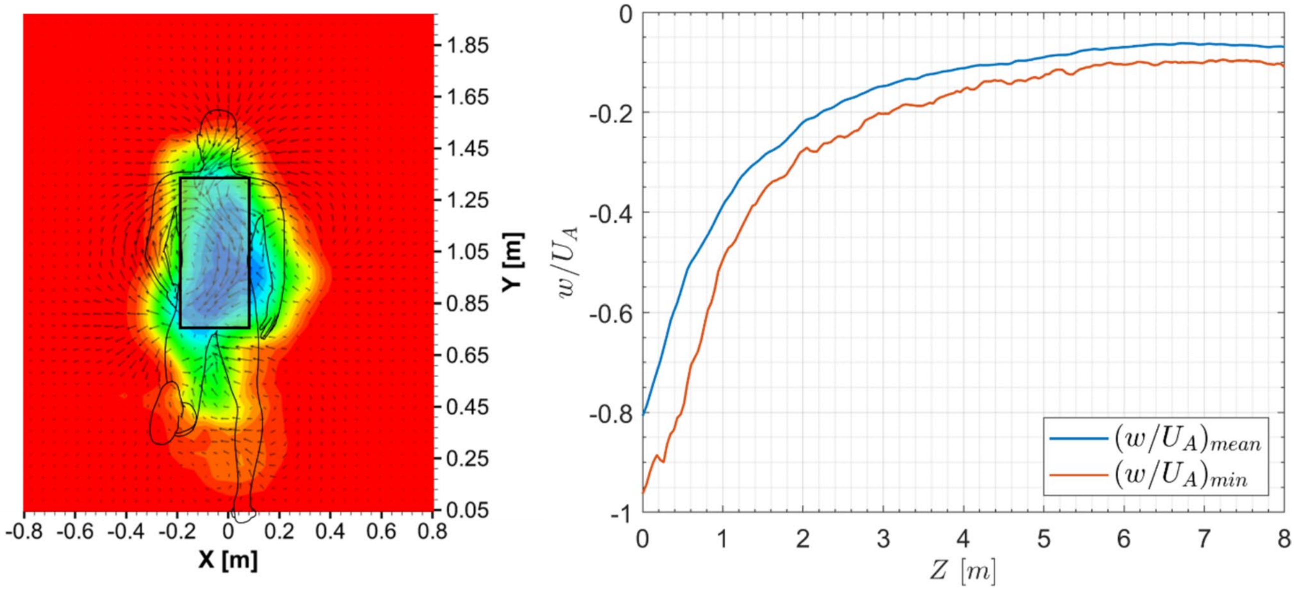

Fig. 8 Evolution of the minimum value of w/U_A along the wake and of the average value of w/U_A evaluated across a rectangular area centred around the athlete's torso (right). The considered rectangular area is highlighted on the left

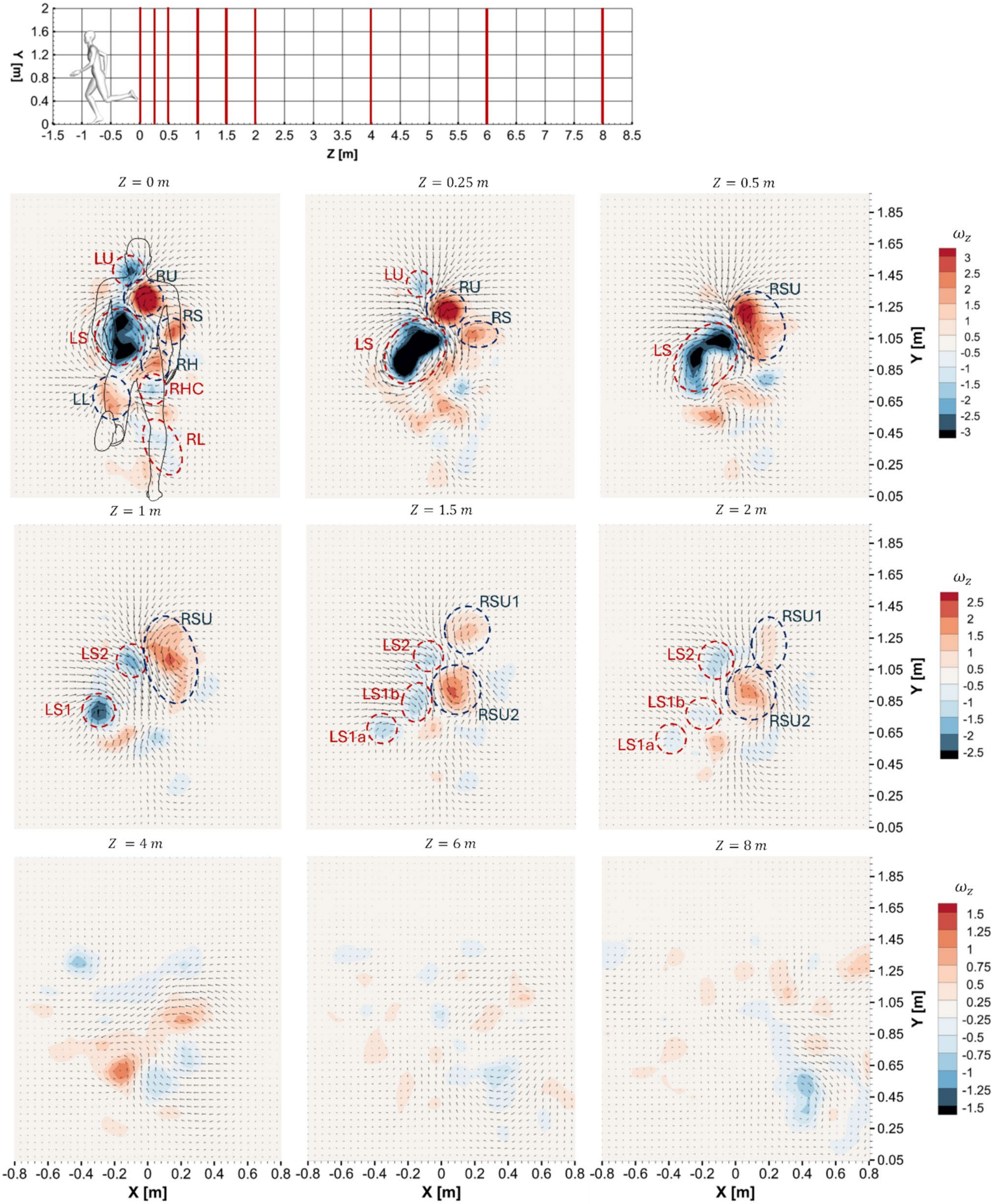

Fig. 9 Evolution of the ensemble-averaged streamwise vorticity component $\boldsymbol{\omega}_z$ in the XY-plane along the wake at Z=0, 0.25, 0.5, 1, 1.5, 2, 4, 6 and 8 m. The main vortical structures identified are highlighted

identification of these circulation regions at greater distances in the wake, the latter are only identified at $Z = 0$ m.

3.1.3 Turbulence intensity

To further investigate the characteristics of the runner's wake, Fig. 10 presents the distribution of the ensemble-averaged turbulence intensity I at $Z = 0$, 2 and 4 m, being I computed as the root mean square (RMS) of the velocity fluctuations normalized by the mean athlete velocity U_A.

Figure 10 shows that, at $Z = 0$ m, the regions of highest turbulence intensity are located between the legs, where I exceeds 50% of the athlete's speed, and around the hands, right arm, head, and the left side of the torso, where I assumes values of about 40% of the runner's velocity. Additionally, the turbulence intensity gradually decreases in the wake due to turbulent dissipation, reaching approximately 10% at a downstream distance of 4 m. Since no further decrease or significant variation in turbulence intensity is observed for $Z > 4$ m, its distribution is not shown for these latter distances.

3.1.4 Pressure coefficient

Building on the wake analysis, an initial evaluation of drafting benefits has been conducted based on the velocity deficit in the runner's wake. Another contributing factor to the advantages of drafting is the suction effect induced by negative pressure coefficient values behind the runner. Therefore, to further investigate this phenomenon and, specifically, to identify the regions in the wake primarily responsible for it, the distribution of the pressure coefficient C_p in the wake is analysed.

Figure 11 illustrates the evolution of the ensemble-averaged C_p in the XY-planes along the wake at $Z = 0$, 0.25, 0.5, 1, 1.5, 2, 4, 6 and 8 m. For clarity, the low-pressure regions discussed in the text are highlighted using circular shapes and corresponding labels. Furthermore, since the pressure coefficient values decrease with increasing the distance behind the runner, the range of C_p in the colorbars has been changed with the increase of Z.

At $Z = 0$ m, three distinct low-pressure regions are observed: one between the left side of the torso and the inner part of the left arm (LS), one similarly formed on the right side of the torso (RS), and one on the upper part of the athlete's back, just below the head (RU). The formation of these regions is associated with the corresponding vortical structures, which are denoted by the same labels in Fig. 9. As the wake develops, the positions of these low-pressure regions evolve until pressure recovery occurs. Specifically, the LS region is the only low-pressure area that persists further downstream, shifting slightly downward as a result of the downwash at the top of the wake, and still identifiable up to $Z = 1$ m. Afterwards, due to turbulent dissipation, the low pressure structures cannot be identified anymore and the pressure coefficient magnitude decreases to below $\left|C_p\right| = 0.1$ for $Z \geq 2$ m.

The negative pressure coefficient values and the resulting suction effect, together with the velocity deficit in the runner's wake, are the primary factors driving the use of drafting to reduce the drag of runners. To further support this statement, Fig. 12 shows the evolution along the wake of the total pressure coefficient, static pressure coefficient and dynamic pressure coefficient averaged across the rectangular region shown on the left, which is consistent with

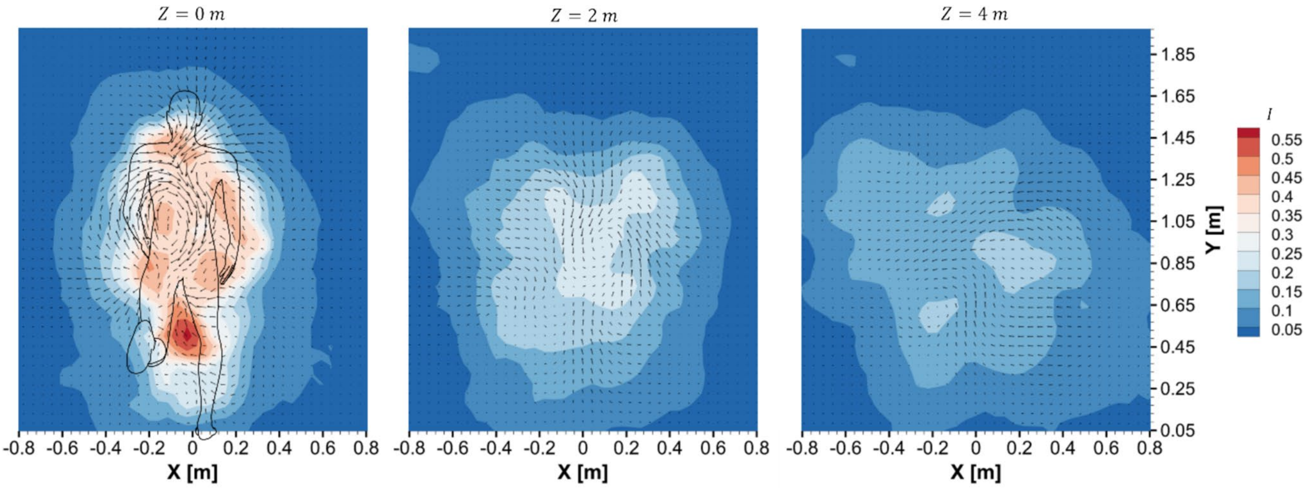

Fig. 10 Evolution of the ensemble-averaged turbulence intensity I in the XY-plane along the wake at $Z = 0$, 2 and 4 m

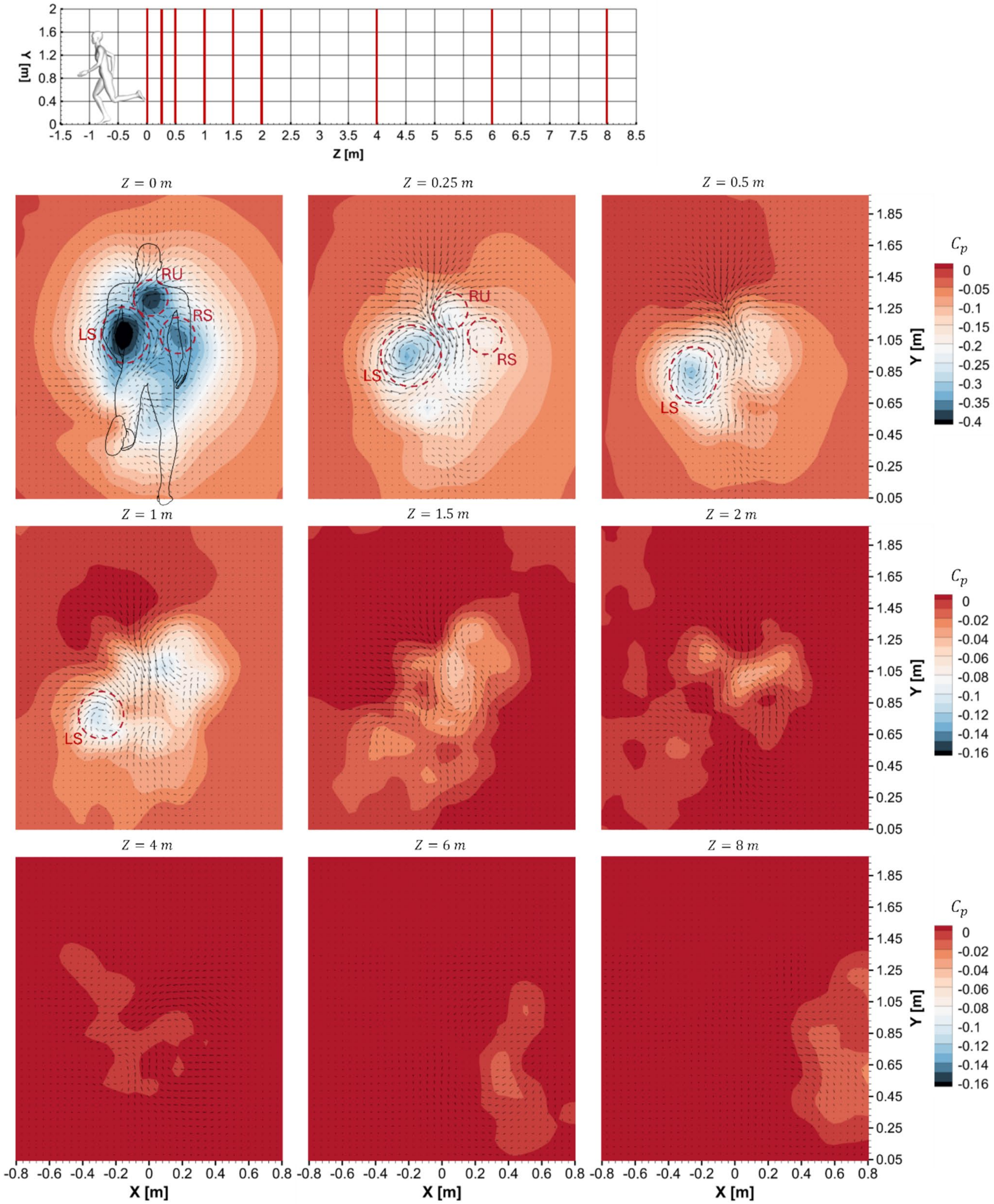

Fig. 11 Evolution of the ensemble-averaged pressure coefficient C_p in the XY-plane along the wake, at $Z=0$, 0.25, 0.5, 1, 1.5, 2, 4, 6 and 8 m. The low-pressure regions identified are highlighted

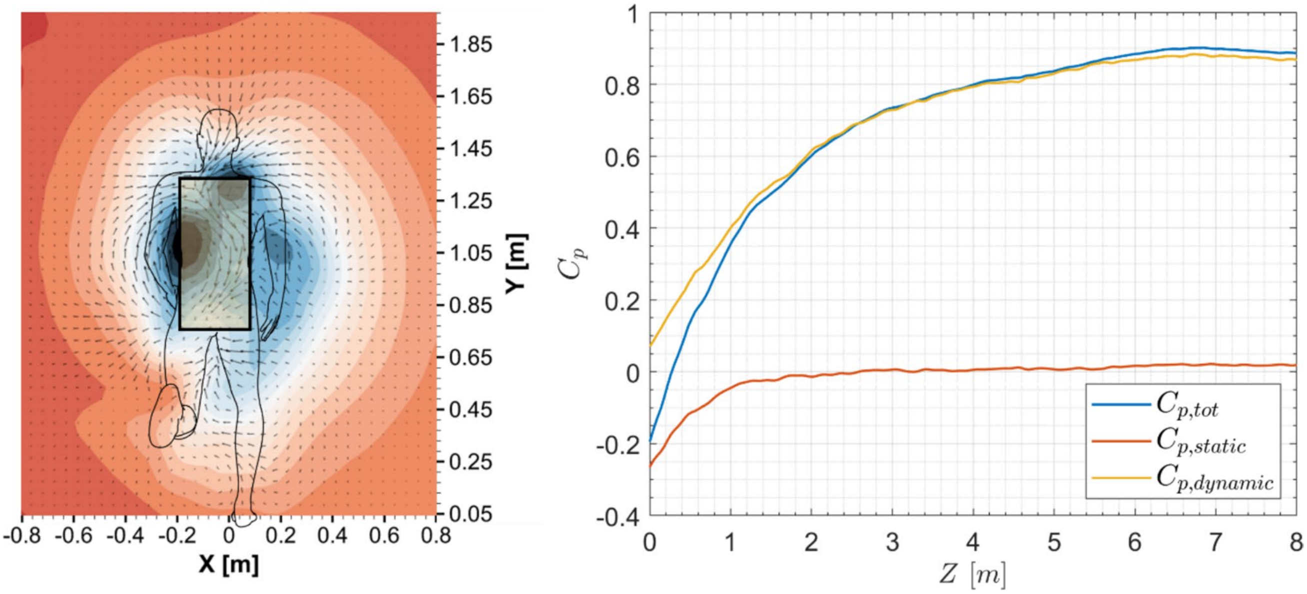

Fig. 12 Evolution of the ensemble-averaged $C_{p,tot}$, $C_{p,static}$ and $C_{p,dynamic}$ averaged across a rectangular area centred around the athlete's torso (right). The considered rectangular area is highlighted on the left

the one used in Fig. 8; the dynamic pressure coefficient is computed in the athlete reference frame.

Figure 12 shows that the static pressure recovers faster than the dynamic pressure in the wake. Specifically, the static pressure coefficient reaches zero at approximately $Z = 2$ m, while the dynamic pressure coefficient reaches a value of 0.8 at $Z = 4$ m. Notice that the total pressure coefficient is the sum of the static and dynamic pressure coefficients and, in the athlete frame of reference, it tends to 1 for increasing distances downstream of the athlete. Because the drag benefit in drafting mainly stems from the reduction in total pressure in front of the trailing athlete (Spoelstra et al. 2021; Terra et al. 2023), it can be concluded that the trailing runner benefits from a 20% drag reduction at 4 m distance, which reduces to 10% beyond 6 m distance. Clearly, the largest drag benefits occur in close proximity to the leading runner, which agrees with the findings of Schickhofer and Hanson (2021) and Beaumont et al. (2021): in particular, for a 1 m distance between the two runners, the trailing runner sees a relative free-stream velocity of 0.6 U_A (see Fig. 8), which results in a free-stream dynamic pressure of 0.36 ($\frac{1}{2}\rho U_\infty^2$) and hence in a drag reduction exceeding 60%.

3.2 Estimation of the drag area

Following the review article of Crouch et al. (2017) on cycling aerodynamics, the drag results are illustrated in terms of the drag area C_DA, evaluated as described in Sect. 2.3.

Figure 13 illustrates the evolution of the ensemble-averaged drag area C_DA_{total} along the wake, decomposed into its momentum (C_DA_{momentum}), pressure (C_DA_{pressure}) and Reynolds stress (C_DA_{RS}) contributions. Physically, the time-averaged drag of the runner is constant and is independent on the location where the conservation of momentum is applied. However, the streamwise evolution of C_DA in Fig. 13 reveals variations depending on the measurement plane. Indeed, in proximity of the athlete, the total drag area reaches its highest value, primarily due to the dominant contribution of the pressure term. It is nevertheless noticed that, in the near wake (i.e. $Z < 1$ m),

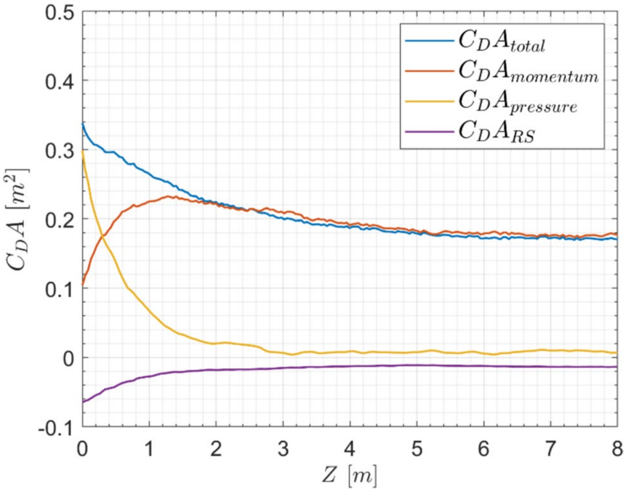

Fig. 13 Evolution of the ensemble-averaged drag area along the wake. The total value of C_DA and the contributions of the momentum term, pressure term and Reynolds stress term are reported

the drag area is overestimated, likely due to uncertainties in the measured pressure field, where fluctuations remain significant. With the increase of the distance behind the runner, as also observed for a sphere (Terra et al. 2017), the pressure contribution to C_DA rapidly decreases, until at $Z \cong 2$ m the momentum contribution becomes the primary component of the total drag area. At this point, the total C_DA reaches a value of approximately 0.22 m^2, though it exhibits a gradual and minor decrease as the streamwise distance further increases. This trend is attributed to the interaction of the flow with the ground, which dissipates momentum and contributes to a progressive underestimation of the aerodynamic drag at larger distances in the wake. Furthermore, as shown by the wake analysis, while the near wake is strongly affected by the instantaneous posture of the athlete, further downstream turbulent mixing leads to a statistically stable wake structure, such that the drag area evaluated in this region provides a meaningful estimate of the aerodynamic drag.

Regarding the Reynolds stress contribution to the drag area, Fig. 13 reveals that C_DA_{RS} exhibits higher values in proximity to the athlete, to progressively decrease until converging to a value of -0.02 m^2 at a distance of approximately 2 m in the wake. Indeed, due to the large-scale LPT measurement uncertainty, the Reynolds stress term is overestimated, resulting in an underestimation of the drag area of approximately 0.02 m^2.

To provide further insight, Fig. 14 presents the variation of the momentum contribution to the drag area in the runner's wake over a distance ranging between 2 and 4 m; data from the five runs of the same athlete whose wake was examined in the previous section are analysed.

For 2 m $\leq Z \leq$ 4 m, the momentum contribution to the drag area exhibits only minor fluctuations, with an average value of 0.22 m^2 over the analysed distance range. Moreover, Fig. 14 shows that the variation between the maximum and minimum values of C_DA across the five runs is approximately 15%, indicating a relatively small spread in the results.

3.2.1 Influence of the athletes' height on the drag area

This section examines the effects of the athletes' height on the wake flow and the corresponding drag area.

To provide insight into the influence of height on the overall wake structure, Fig. 15 presents the distribution of the ensemble-averaged streamwise velocity component w/U_A at $Z = 0$ m for the six athletes who participated in the experimental campaign. Each w/U_A distribution corresponds to an individual athlete and, therefore, to a specific height. Additionally, the corresponding C_DA value has been computed for each athlete.

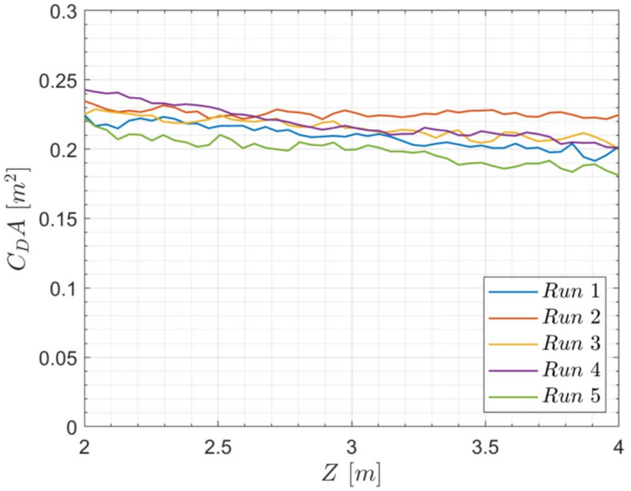

Fig. 14 Variation of the momentum contribution to the drag area for 2 m $\leq Z \leq$ 4 m, for the five analysed runs of an individual athlete

Figure 15 reveals that taller athletes generate a taller wake, leading to increased drag area values. It is observed that the overall wake structure remains largely consistent across different athletes. Several recurring flow features can indeed be identified, including the downwash effect from the head, the upwash effect from the hips, and the low-velocity region downstream of the standing leg. These similarities indicate that, despite differences in height, key aerodynamic flow structures persist for different runners and so, that the differences in the aerodynamic drag are primarily stemming from the differences in the frontal area of the athlete.

Following the approach of Pecchiari et al. (2023), Fig. 16 illustrates the variation of C_DA as a function of height squared for the six athletes involved in the experimental campaign. In accordance with privacy agreements, each height value is reported within a range of ± 0.02 m. Furthermore, together with the results obtained in the present study, also the experimental results on running athletes of Pecchiari et al. (2023) and the numerical results on static models of Beaumont et al. (2022) are shown in Fig. 16. Specifically, the experimental data reported by Pecchiari et al. (2023) were obtained from eight male runners, with the drag area evaluated at running velocities in the range 4–5 m/s, while the numerical data of Beaumont et al. (2022) are based on CFD simulations of five static male runner models. Although Beaumont et al. (2022) investigated a wide range of running speeds (10–40 km/h), the data reported in Fig. 16 correspond to a speed of 30 km/h, which is the closest value to the running speed considered in this work.

For the present study, as well as for the works of Pecchiari et al. (2023) and Beaumont et al. (2022), the trend observed in Fig. 16 indicates a linear increase in C_DA with the athletes' height squared. In all three datasets, the slope of the fitting line is approximately 0.14, with Root Mean

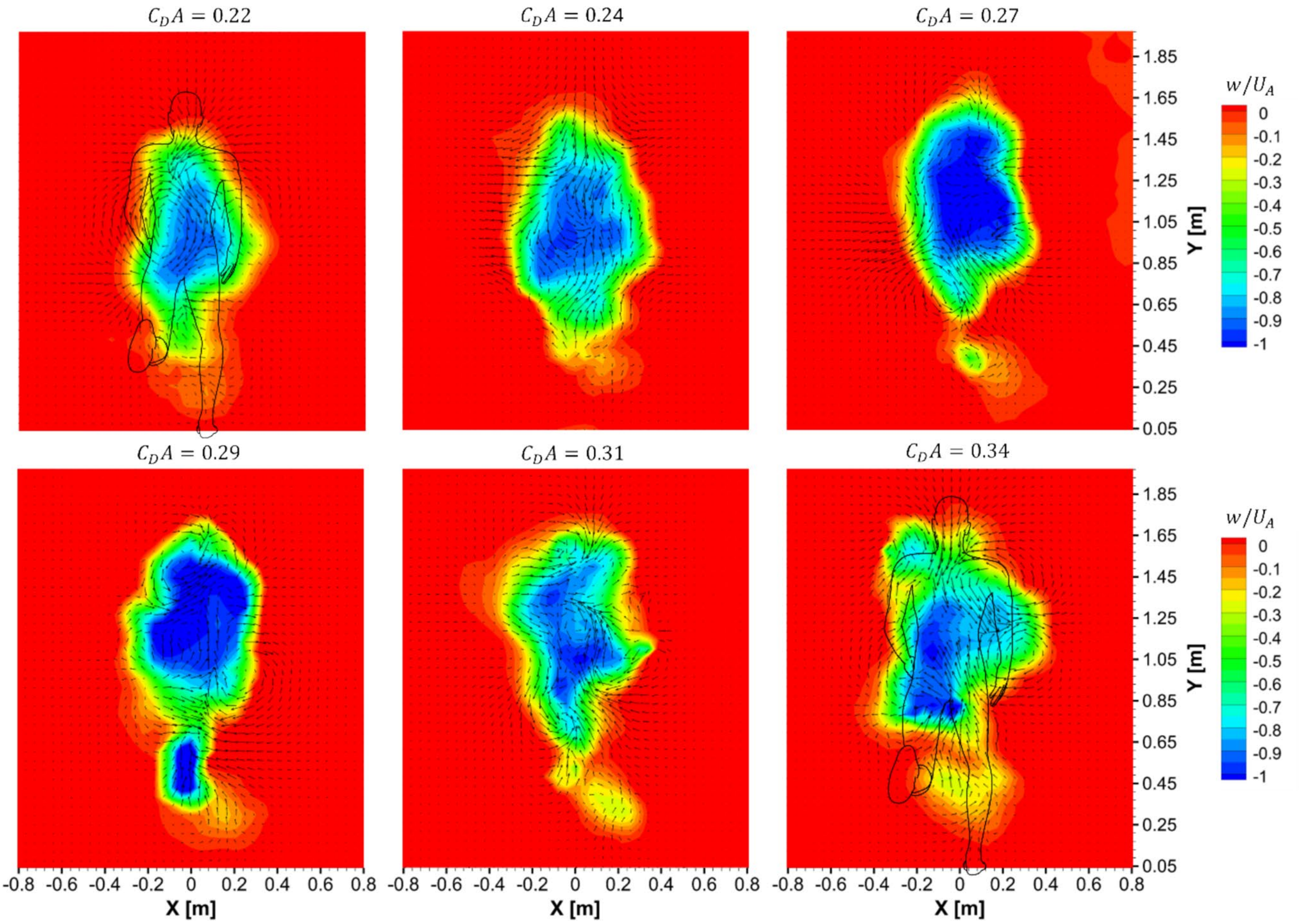

Fig. 15 Distribution of the ensemble-averaged w/U_A at Z = 0 m for the six athletes involved in the experimental campaign

Square Error (RMSE) values of 0.019 for the present work, 0.025 for Pecchiari et al. (2023) and 0.007 for Beaumont et al. (2022). Within the specified height range, the increase of C_DA with the runners' height can be primarily attributed to the larger frontal area of taller athletes. However, the C_DA values reported by Pecchiari et al. (2023) and by Beaumont et al. (2022) are approximately 30–40% greater than those found in the present study. This difference can be attributed to both experimental and aerodynamic factors. Specifically, the higher C_DA values reported by Pecchiari et al. (2023) may be related to the garments used during the experiments. Indeed, participants were instrumented with wearable metabolic equipment (e.g. backpack and face mask), which may also have affected their running posture. The particular running apparel (e.g. tight/loose, short/long sleeve) was not mentioned. In the present work, low-drag aero suits were worn. It is well known that tight fitting clothing can decrease the aerodynamic drag by over 10% in comparison with loose apparel (Blocken et al. 2024). Low-drag suits can decrease the drag by a similar amount (Brownlie et al. 2016). Hence, the differences in garments can well explain the relatively large difference in aerodynamic drag between the present study and that of Pecchiari et al. (2023). Conversely, the

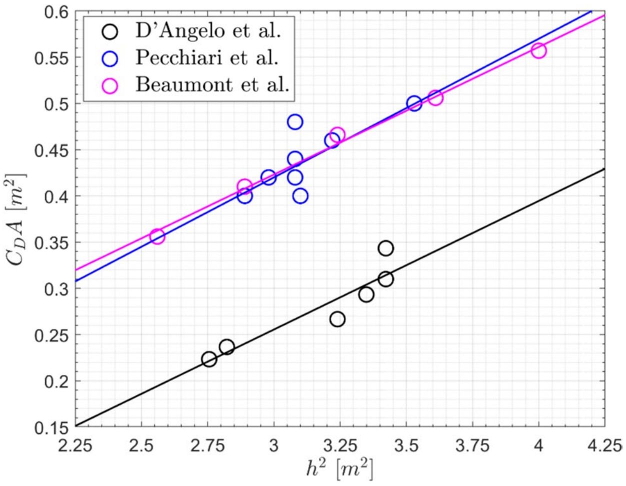

Fig. 16 Effect of the athletes' height on the drag area

difference between the results of the present study and those of Beaumont et al. (2022) can be explained by the static configuration of their runner models. Indeed, considering that the overall uncertainty of the drag estimation in the present experiments is within 5% (see Sect. 2.3), the difference in C_DA values is attributed to the unsteadiness of the running motion. As an example, the lower leg is nearly stationary relative to the air when standing on the floor, resulting in a negligible velocity deficit in the wake (see Sect. 3.1.1) and, consequently, a minimal contribution to the aerodynamic drag of the athlete. When considering a static athlete model, such variation in the velocity among the limbs is not present. This further highlights the importance of performing drag measurements on moving athletes rather than static ones.

Furthermore, the C_DA values found in the present study are in close agreement with those predicted by the analytical model of Mureika (2001), who estimated a C_DA of 0.23 m^2 for an 80 kg sprinter running at approximately 11 m/s, and with the numerical simulations of Hu et al. (2026), who found a $C_DA \approx 0.285$ m^2 for a 1.76 m tall static mannequin at 10 m/s and a blockage ratio of about 4.8%. These results confirm that the drag area values measured in the present on-site experiments are consistent with existing analytical and numerical estimates.

4 Conclusions

This study investigates the aerodynamics of professional sprinters through an on-site analysis employing the Ring of Fire (RoF) methodology. Using Lagrangian Particle Tracking (LPT) with helium-filled soap bubbles as tracer particles, time-resolved flow field data was collected and analysed. The data was processed using the Shake-the-Box (STB) algorithm implemented in DaVis 10, enabling a detailed characterization of the wake flow structures generated by athletes sprinting at an average speed of 8 m/s, corresponding to a Reynolds number of 2×10^5, based on the shoulder width. The findings of the present work provide a comprehensive understanding of sprinting aerodynamics during the dynamic motion of the athlete, addressing a gap in the existing literature. While previous studies performed numerical simulations and experimental measurements on static human models, the present analysis investigates the wake flow topology of moving sprinters. Specifically, the ensemble-averaged streamwise velocity and vorticity fields, as well as the pressure coefficient distribution in the wake, are analysed to characterize the wake flow dynamics. Furthermore, the aerodynamic drag of sprinters is assessed by applying momentum conservation within a control volume containing the athlete and moving with him; the results are illustrated in terms of the drag area. Additionally, the influence of the athletes' height on the drag area and on the general wake flow topology is investigated.

The findings of the present study provide a comprehensive understanding of sprinting aerodynamics, offering valuable insights into the influence of the athletes' body morphology on aerodynamic performance and optimal drafting distances. Specifically, the results obtained show that, in proximity to the athlete, the wake shape resembles the runner's body, with the torso exerting the most significant influence on the wake flow topology. By increasing the distance from the runner, the wake progressively shortens in height and expands in width, eventually leading to a bifurcation in the streamwise velocity field. This results in the formation of two distinct regions of peak velocity, between which the streamwise velocity recovers to freestream levels. Furthermore, a downwash effect from the head and an upwash effect from the hips are consistently observed in the near wake.

The analysis of the streamwise vorticity distribution along the wake reveals that vorticity structures consistently form across different athlete passages and can be directly linked to the body parts responsible for their generation. These vortical structures have also been correlated with the low-pressure regions identified in the wake, therefore allowing for a deeper understanding of the wake flow topology.

Furthermore, the combined analysis of velocity deficit and pressure coefficient variation along the wake offers valuable insights into drafting advantages. The results confirm that drafting benefits are greatest up to approximately 1 m, where a drag reduction of about 60% is observed, while they remain significant up to a distance of 8 m with a drag reduction of approximately 10%. Moreover, the results confirm a linear increase in drag area with the athlete's height squared, as taller athletes exhibit a larger projected frontal area and consequently generate a higher drag area. It is also remarkable that the C_DA values found in the present work are 30–40% lower than most of the values reported in previous experimental studies conducted on running athletes and numerical investigations based on static mannequins, a difference attributed to the higher experimental realism of the present on-site measurements. This result further highlights the importance of performing experimental and numerical studies that capture the full unsteadiness of real running conditions.

Author contributions Cristina D'Angelo: Conceptualization, Methodology, Software, Validation, Formal analysis, Investigation, Data Curation, Writing—Original Draft. Michael Buszek: Investigation, Formal Analysis, Data Curation. Wouter Terra: Conceptualization, Methodology, Investigation, Formal Analysis, Data Curation, Writing—Review & Editing, Funding acquisition, Project administration, Software, Supervision. Andrea Sciacchitano: Conceptualization, Methodology, Investigation, Writing—Review & Editing, Supervision, Funding acquisition, Software.

Funding Research funding provided by the Dutch Research Institution NWO. Open access funding provided by Università degli Studi di Napoli Federico II within the CRUI-CARE Agreement.

Data availability The data underlying this study are available in the 4TU.ResearchData repository (https://doi.org/10.4121/33bbeae9-fec4-49c9-99b8-4a5f9ea0bcbd).

Declarations The authors declare no competing interests.

References

Agüera N, Cafiero G, Astarita T, Discetti S (2016) Ensemble 3D PTV for high resolution turbulent statistics. Meas Sci Technol 27(12):124011

Arnol'd VI 2013 Mathematical methods of classical mechanics, Springer Science \& Business Media

Ashton J, Jones PA (2019) The reliability of using a laser device to assess deceleration ability. Sports 7(8):191

Beaumont F, Legrand F, Bogard F, Murer S, Vernede V, Polidori G (2021) Aerodynamic interaction between in-line runners: new insights on the drafting strategy in running. Sports Biomechanics 23(11):1–16

Beaumont F, Delouis P, Polidori G (2022) Numerical aerodynamic database in elite male runners. Int J Sports Sci Coach 17:880–884

Blocken B, Malizia F, Laguna P, Marshall D, Bell D, Marchal T (2024) Numerical-physical modelling of the long jump flight of female athletes: impact of jump style, hairstyle and clothing. J Wind Eng Ind Aerodyn 252:105837

Brownlie L, Aihara Y, Carbo J Jr, Harber E, Henry R, Ilcheva I, Ostafichuk P (2016) The use of vortex generators to reduce the aerodynamic drag of athletic apparel. Procedia Eng 147:20–25

Chowdhury H, Alam F, Subic A (2010) Aerodynamic performance evaluation of sports textile. Procedia Eng 2(2):2517–2522

Crouch T, Burton D, Brown N, Thompson M, Sheridan J (2014) Flow topology in the wake of a cyclist and its effect on aerodynamic drag. J Fluid Mech 748:5–35

Crouch TN, Burton D, LaBry ZA, Blair KB (2017) Riding against the wind: a review of competition cycling aerodynamics. Sports Eng 20:81–110

Forte P, Sousa N, Teixeira J, Marinho D, Monteiro A, Bragada J, Morais J, Barbosa T (2022) Aerodynamic analysis of human walking, running and sprinting by numerical simulations. Acta Bioeng Biomech 24(3)

Gibertini G, Donato G (2008) Cycling aerodynamics. Springer

Hill AV (1928) The air-resistance to a runner. Proc R Soc Lond B Biol Sci 102(718):380–385

Hu X, Malizia F e B. Blocken 2026 CFD simulations of running aerodynamics: impact of computational parameters J Wind Eng Ind Aerodynamics 268 106271

Huttig S, Gericke T, Sciacchitano A and Akkermans RA 2023 "Automotive on-road flow quantification with a large scale Stereo-PIV setup," in proceedings of the 15th international symposium on particle image velocimetry

Kim J, Lee S, Ho V-T, Shin D, Ryu J (2023) Effects of speed and posture on aerodynamic characteristics of running and required power. Int J Appl Mech 15(1):2250105

Krajnović S (2011) Flow around a tall finite cylinder explored by large eddy simulation. J Fluid Mech 676:294–317

Kurtulus D, Scarano F, David L (2007) Unsteady aerodynamic forces estimation on a square cylinder by TR-PIV. Exp Fluids 42:185–196

Mureika J (2001) A realistic quasi-physical model of the 100 m dash. Can J Phys 79(4):697–713

Pecchiari MM, Legramandi MA, Gibertini G, Cavagna GA (2023) Still air resistance during walking and running. Proc Biol Sci 290(2013):20231763

Rostamy N, Sumner D, Bergstrom D, Bugg J (2012) Local flow field of a surface-mounted finite circular cylinder. J Fluids Struct 34:105–122

Sætran L, Oggiano L (2008) Skin suit aerodynamics in speed skating. In: Sport aerodynamics, pp 93–105

Scarano F, Ghaemi S, Caridi GCA, Bosbach J, Dierksheide U, Sciacchitano A (2015) On the use of helium-filled soap bubbles for large-scale tomographic PIV in wind tunnel experiments. Exp Fluids 56:1–12

Schanz D, Gesemann S, Schröde A (2016) Shake-The-Box: lagrangian particle tracking at high particle image densities. Exp Fluids 57:1–27

Schickhofer L, Hanson H (2021) Aerodynamic effects and performance improvements of running in drafting formations. J Biomech 110457:122

Spoelstra A, de Martino Norante L, Terra W, Sciacchitano A, Scarano F (2019) On-site cycling drag analysis with the ring of fire. Exp Fluids 60:1–16

Spoelstra A, Hirsch M, Sciacchitano A, Scarano F (2021) Uncertainty assessment of the ring of fire concept for on-site aerodynamic drag evaluation. Meas Sci Technol 32(4):044004

Spoelstra A, Terra W, Sciacchitano A (2023) On-site aerodynamics investigation of speed skating. J Wind Eng Ind Aerodyn 239:105457

Terra W, Sciacchitano A, Scarano F (2017) Aerodynamic drag of a transiting sphere by large-scale tomographic-PIV. Exp Fluids 58:1–14

Terra W, Sciacchitano A, Scarano F, van Oudheusden B (2018) Drag resolution of a PIV wake rake for transiting models. Exp Fluids 59:1–6

Terra W, Spoelstra A, Sciacchitano A (2023) Aerodynamic benefits of drafting in speed skating: estimates from in-field skater's wakes and wind tunnel measurements. J Wind Eng Ind Aerodyn 233:105329

van Oudheusden B (2013) PIV-based pressure measurement. Meas Sci Technol 24(3):032001

Wieneke B (2008) Volume self-calibration for 3d particle image velocimetry. Exp Fluids 45(4):549–556

Zhang Y, Ke P, Hong P (2023) Aerodynamic drag reduction analysis of race walking formations based on CFD numerical simulations and wind tunnel experiments. Appl Sci 19:13